Ultrathin g-C$_3$N$_4$ nanosheets coupled with carbon nanodots as 2D/0D composites for efficient photocatalytic H$_2$ evolution

Qiong Liu, Tianxiang Chen, Yarong Guo, Zhengguo Zhang, Xiaoming Fang*

Key Laboratory of Enhanced Heat Transfer and Energy Conservation, The Ministry of Education, School of Chemistry and Chemical Engineering, South China University of Technology, Guangzhou 510640, China

ABSTRACT

Carbon nanodots synthesized from rapeseed flower bee pollens were used to couple with ultrathin g-C3N4 nanosheets for preparing the 2D/0D type photocatalysts by a hydrothermal method. The g-C$_3$N$_4$ nanosheets (UCN) obtained from ammonium chloride blowing dicyandiamide methods exhibit ultrathin two-dimension structure with a series of hollow spherical structures, and CQDs are well dispersed and uniformly anchored into the UCN network via π-π stacking interactions. The incorporation of CQDs can effectively expand visible light absorption regions via photosensitization and suppress the recombination of photo-induced carriers. Time-resolved fluorescence spectroscopy, electron paramagnetic resonance technology and photoelectrochemical measurements together reveal that CQDs serve as electron transfer mediation to facilitate charge separation and extend the lifetime of photo-induced carriers. The UCN/CQDs-0.2% composite has the optimal H$_2$ evolution of 88.1 μmol/h, 9.79, 3.02 and 1.91 folds of bulk g-C$_3$N$_4$ (BCN), pristine UCN and BCN/CQDs-0.2%, respectively. Consequently, the UCN/CQDs composites exhibit high photocatalytic activity of hydrogen release under the visible light irradiation.

© 2016 Elsevier B.V. All rights reserved.

1. Introduction

Solar radiation is the main renewable energy source for human being. Semiconductor-based photocatalysis has been recognized as one of the most promising technologies to solve the energy crisis and environment pollution via photocatalytic water splitting and photodegradation of contaminants using solar energy [1–3]. Visible-light response photocatalysts with high activity and good stability are essential for practical applications of the photocatalysis technology [4–6]. Although various visible-light response photocatalysts, including metal nitrides [7,8], metal chalcogenides [9–11], (oxy)nitrides [12] and (oxy)sulfides [13], have been demonstrated to be able to produce hydrogen through water splitting, most of them suffer from poor chemical or thermal stability [14]. Graphitic carbon nitride (g-C$_3$N$_4$) is a metal-free polymeric semiconducting material, which possesses a two-dimensional structure consisting of π-conjugated graphitic planes through the sp2 hybridization of carbon and nitrogen [15–17]. The advantages of a relatively narrow band gap (∼2.7 eV), suitable band positions and high chemical stability make g-C$_3$N$_4$ a promising photocatalyst for hydrogen production through water splitting [14,18,19]. Unfortu-

nately, pristine g-C$_3$N$_4$ exhibits a limited visible light absorption region of less than 460 nm as well as a poor quantum efficiency, resulting in its low photocatalytic activity [20,21]. Therefore, it is of significance to develop novel g-C$_3$N$_4$ based photocatalysts with wide visible light response and high photocatalytic activity.

Up to now, several approaches have been explored to improve the photocatalytic activity of g-C$_3$N$_4$, which mainly include doping with metal [22–25] and/or nonmetal ions [26–29], construction of heterojunctions with other semiconductors [30,31], copolymerization with organic molecules [32,33], and photosensitization with dyes [34,35]. However, certain drawbacks still involve in these strategies. Specifically, the isolated states formed by doping possibly act as recombination centers for the photogenerated carriers [36]; Although heterojunction structures facilitate the separation of photo-induced hole-electron pairs, they usually sacrifice their redox ability [37]; The copolymerization with structure-matching organic additives is a unique way for modifying the band gap and positions of g-C$_3$N$_4$, but only a small amount of organic molecules can anchor into the texture edge of g-C$_3$N$_4$ [38–41]; The dye-sensitized photocatalysts generally suffer from a decline in photocatalytic activity due to the instability of dye molecules under light irradiation [42]. Consequently, although extensive efforts have been made toward developing the g-C$_3$N$_4$-based photocatalysts with enhanced photocatalytic activity, the actual performance of those photocatalysts have not satisfied the application require-
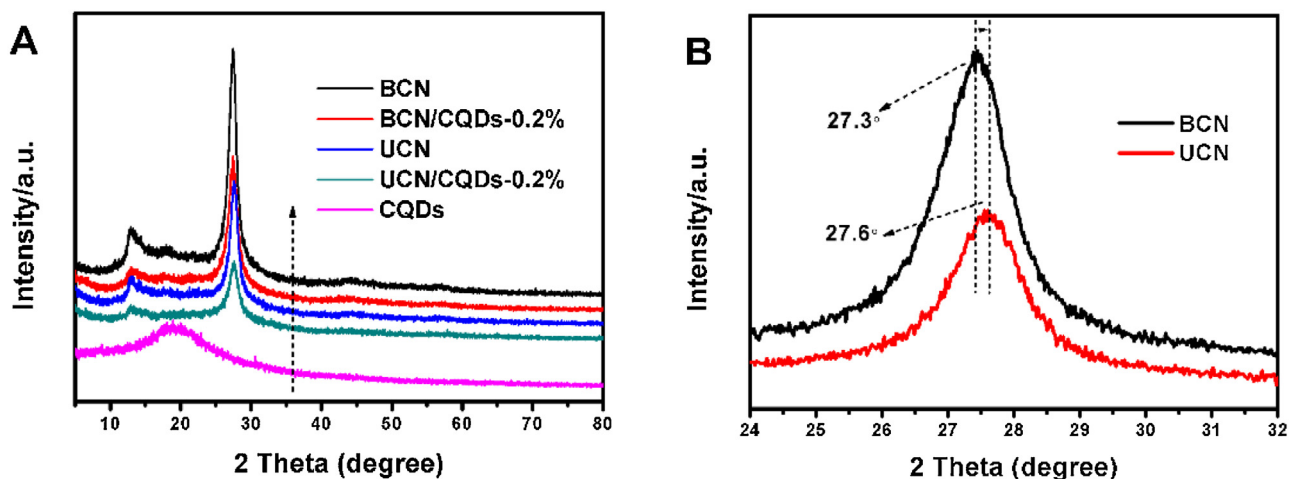
Fig. 1. XRD patterns of BCN, UCN, BCN/CQDs-0.2%, UCN/CQDs-0.2% and CQDs.
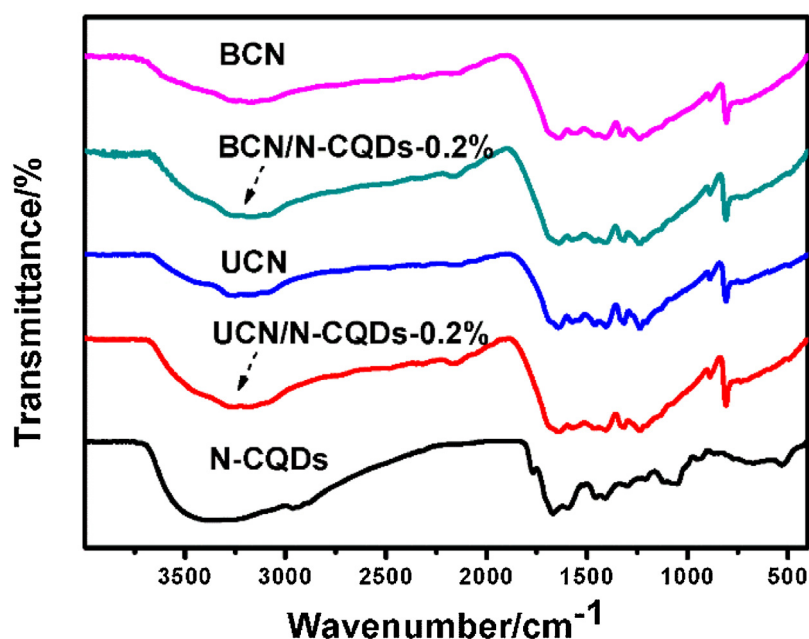

Fig. 2. FT-IR spectra of BCN, UCN, BCN/CQDs-0.2%, UCN/CQDs-0.2% and CQDs.

ment yet. Apparently, more effective strategies need to be explored for developing the high-performance g-C$_3$N$_4$-based photocatalysts.

Carbon quantum dots (CQDs), a novel kind of carbon nanomaterials, predominantly consist of the particles with sizes of 2–10 nm and retain the typically π-π* stacking transition of aromatic sp2 hybridized graphitic carbon [43]. It has been reported that CQDs exhibit unique photo-physical properties, which not only render their excited wavelength dependent photoluminescence behavior, but also endow them a promising photosensitizer for broadening optical absorption as well as an excellent electron acceptor [44–46]. Recently, the integration of CQDs with photocatalysts, such as TiO$_2$ [47,48], CdS [49], Fe$_2$O$_3$ [50], BiVO$_4$ [51], and Cu$_2$O [52], has been demonstrated to have the function of enhancing the activity of those photocatalysts by increasing their visible-light absorption region and reducing the photo-induced carrier recombination simultaneously. More significantly, CQDs have been also coupled with g-C$_3$N$_4$ to construct environmental friendly metal-free composite photocatalysts with improved performance [53]. Liu et al. [54] reported that CQDs surface-sensitized g-C$_3$N$_4$ exhibited

an impressive activity for photocatalytic water splitting, resulting from its visible light absorption beyond 600 nm and high quantum efficiency. Gao et al. [55] theoretically studied the underlying photocatalytic mechanism of the carbon nanodot decorated g-C$_3$N$_4$, and found that a type-II van der Waals heterojunction could be formed between carbon nanodots and g-C$_3$N$_4$, in which carbon nanodots also acted as a spectral sensitizer. The more recent research by Zhang et al. revealed that the impregnation of carbon nanodots onto g-C$_3$N$_4$ promoted phenol degradation by yielding more holes, •O$_2$ and •OH radicals [56,57]. All the above researches suggested that the coupling of CQDs with g-C$_3$N$_4$ is a very efficient way for developing high-performance g-C$_3$N$_4$ based photocatalysts. Therefore, further investigations need to be carried out on this strategy.

In the current work, ultrathin g-C$_3$N$_4$ nanosheets were used to couple with CQDs, with the purpose of combining two-dimensional (2D) ultrathin g-C$_3$N$_4$ nanosheets with zero-dimensional (0D) CQDs to obtain high-performance g-C$_3$N$_4$ based photocatalysts. The obtained 2D/0D composite photocatalysts were character-
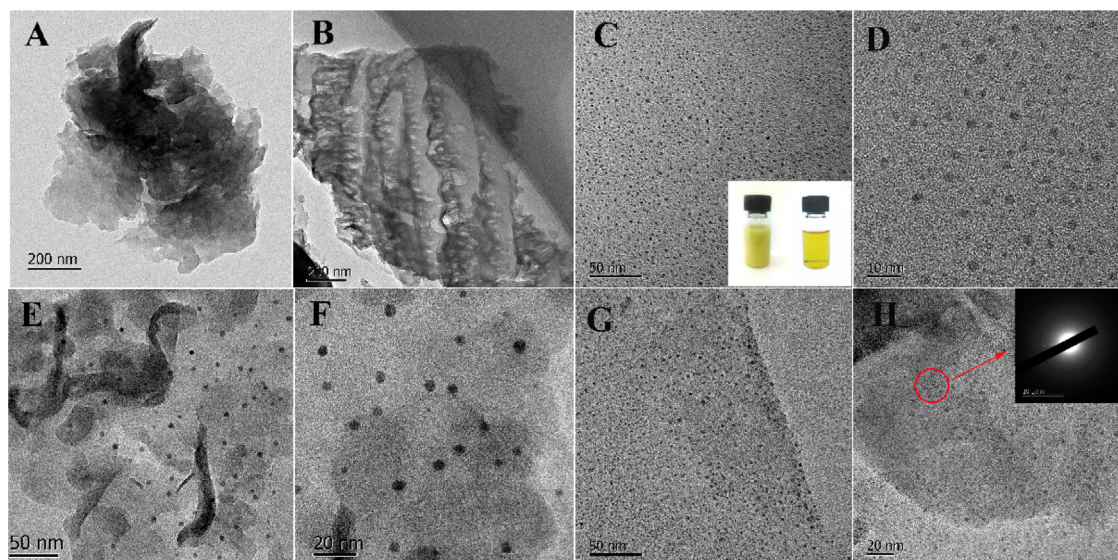
Fig. 3. TEM images of BCN(A), UCN(B), pure CQDs (C, D), BCN/CQDs-0.2% (E, F) and UCN/CQDs-0.2% (G, H). The inset in (C) is the digital photographs of the suspension of rapeseed flower bee pollens (left) and as-obtained solution of pure CQDs (right). The selected area electron pattern (SAED) of UCN/CQDs is the inset of (H).

ized, and their photocatalytic activity for hydrogen production was evaluated. It is found that the CQDs decorated ultrathin g-C_3N_4 nanosheets exhibited high photocatalytic activity, revealing that such a 2D/0D heterojunction architecture can enhance the photocatalytic activity of g-C_3N_4 for hydrogen releasing under visible light irradiation by broadening optical region for light harvesting along with shortening transport distance for electrons trapping.

2. Experimental section

2.1. Sample preparation

2.1.1. Materials

Rapeseed flower bee pollens were purchased from an online store on the Taobao website. Dicyandiamide and ammonium chloride were purchased from Sigma Aldrich Chemical Co., and used without further purification.

2.1.2. Preparation of CQDs

CQDs were prepared from rapeseed flower bee pollens via a hydrothermal method [58]. In a typical process, 1 g of rapeseed flower bee pollens was added in 40 mL of water. After sonication for 30 min, the aqueous solution was transferred into a 50 mL Teflon-lined stainless steel autoclave and maintained at 453 K for 24 h. After the autoclave was naturally cooled to room temperature, the resuled suspension was separated with millipore filter (0.2 μm pore size). The obtained CQDs were dispersed into water to prepare a suspension (10 mg/ml), and the suspension was stored at 4 °C for further application. In addition, a solid sample of the CQDs used for characterization was gained by freeze drying the suspension at 203 K for 48 h.

2.1.3. Preparation of ultrathin CN sheets

Ultrathin g-C_3N_4 nanosheets were prepared according to the previously reported method [16]. Typically, 3 g of dicyandiamide and 15 g of ammonium chloride were dissolved into water under stirring at 353 K. After the aqueous solution had been dried, the obtained mixture was transferred in a muffle furnace followed by being heated to 823 K and maintained for 4 h. The obtained material was milled into powder and donated as UCN. For comparison purpose, bulk g-C_3N_4 was prepared under the identical condition without the addition of ammonium chloride and donated as BCN.

2.1.4. Preparation of UCN/CQDs composites

The UCN/CQDs composites were prepared by a hydrothermal method. Specifically, different amounts of the CQDs suspension were added into 40 mL of ethanol, in which 0.25 g of UCN had been dispersed. After being stirred for 2 h, the mixture suspension was transferred into a 50 mL Teflon-lined stainless steel autoclave and maintained at 393 K for 2 h. The obtained UCN/CQDs composites with different mass fractions of CQDs were collected by centrifugation, washed and dried under vacuum at 333 K for 6 h. In addition, BCN/CQDs with different mass fractions of CQDs were prepared via the same process.

2.2. Characterization

X-ray diffraction (XRD) patterns were recorded by a Bruker D8 advance diffractometer using Cu Kα radiation at a scan rate of 0.02 °/s in the 2θ range from 5° to 80°. The morphologies and microstructures of the samples were observed by a Hitachi S-3700 N scanning electron microscope (SEM) and a JEOL model of JEM2100F transmission electron microscope (TEM). UV–vis diffuse reflectance spectra (DRS) of the samples were obtained on a Shimadzu U-3010 spectrophotometer, and $BaSO_4$ was used as a reflectance standard. Photoluminescence (PL) spectra of the photocatalysts were recorded on a Hitachi F-4600 spectrometer under an excitation wavelength of 375 nm. The X-ray photoelectron spectroscopy (XPS) was conducted on an Ulvac-Phi PHI 5300 ESCA system with Mg Kα source, and the spectra was calibrated using the C 1s peak at 284.6 eV. Electron spin resonance (ESR) signals were investigated on a Bruker model A300 electron paramagnetic resonance spectrometer equipped at room temperature with a 300W Xe lamp as the visible light source. The infrared absorption spectra was investigated using a Bruker Vector 33 Fourier transform infrared (FT-IR) spectrophotometer over the wavenumber range from 400 to 4000 cm^{-1}. The transient photoluminescence (PL) decay spectra was recorded on an Edinburgh PLS980 spectrometer at room temperature. The specific surface area (BET) and pore volume was collected at 77 K using a Micromeritics ASAP 2020 apparatus and porosity analyzer. The particles size was measured by a Malvern Zetasizer Nano ZS analysis meter.
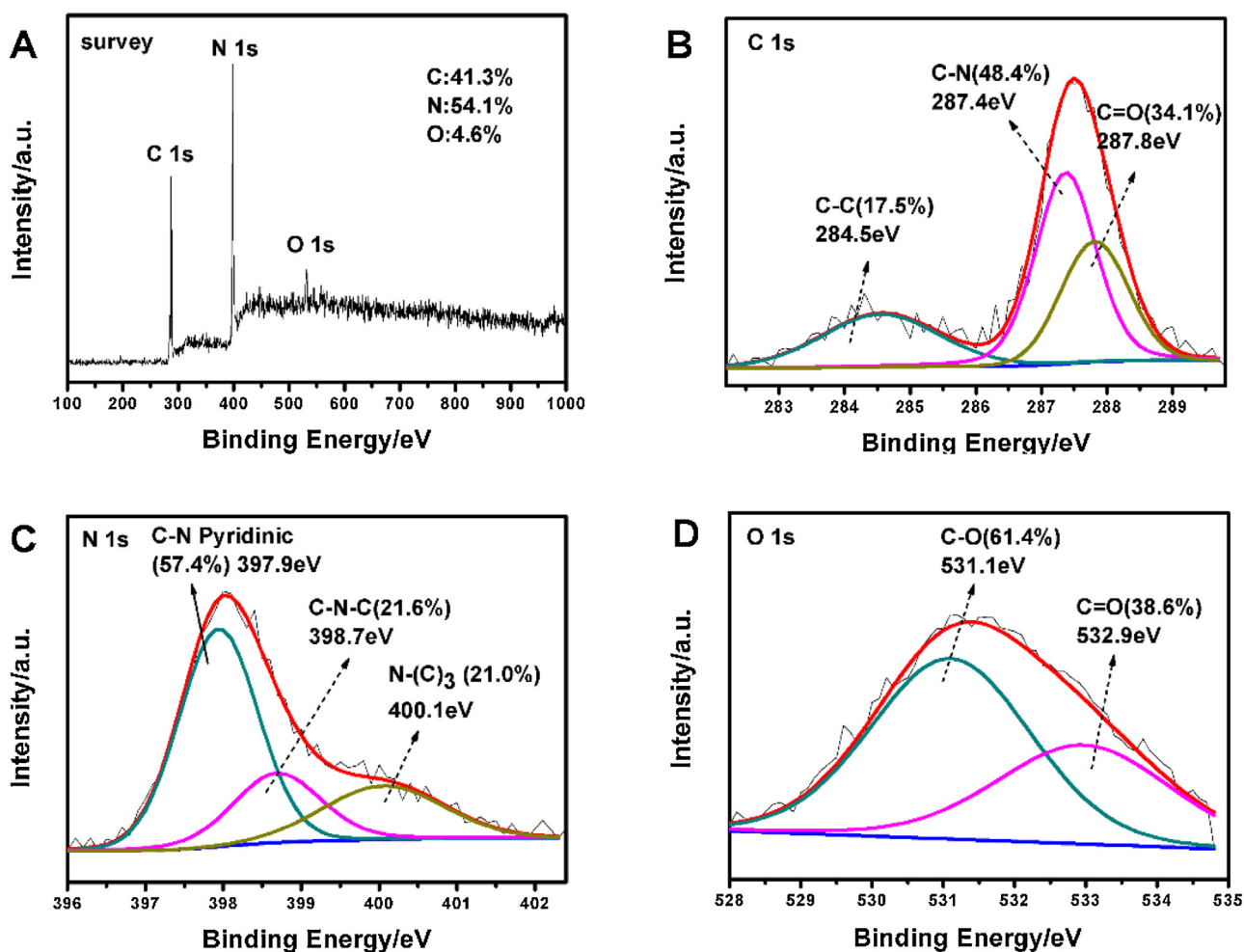
Fig. 4. XPS spectra of UCN/CQDs-0.2% sample: Survey (A), C1s (B), N1s (C), and O1s (D).

2.3. Evaluation of photocatalytic activity for hydrogen production

The photocatalytic water splitting reactions were performed in an outer top-irradiation photoreactor vessel with a closed gas circulation system. Briefly, 0.05 g of the UCN/CQDs composites were dispersed into 100 mL of 5 vol% methanol aqueous solution containing H_2PtCl_6 (Pt, 0.2% wt) used as a cocatalyst. A 300 W Xe-lamp (ProfectLight, PLS-SXE300C) with a 420 nm cutoff filter was used as the visible light source. Before irradiation, the suspension was thoroughly degassed to assure vacuum environment, and the reaction system was maintained at 278 K by flowing cooling water during the reaction. The amount of H_2 product evolved was analyzed with an online gas chromatograph (GC7600, Tian Mei) equipped with a TCD detector, and nitrogen was used as the carrier gas.

2.4. Photoelectrochemical measurement

A working electrode for photoelectrochemical measurement was prepared as follows: 0.1 g of the as-prepared composites were added into an ethanol solution containing 0.01 g ethyl cellulose, followed by being grinded into fine slurries. The electrodes were fabricated by coating the slurries onto FTO glass by the doctor-blading method, followed by drying at 393 K for 1 h. The photocurrent test was carried out on electrochemical analyzer (CorrTest CS350) with a standard three-electrode system, in which Pt wire was used as the counter electrode and Ag/AgCl as the reference electrode. The simulated visible light source was pro-vided by a 300 W Xe lamp with a UV-cutoff filter ($\lambda > 420$ nm). 0.25 M sodium sulfide/0.35 M sodium sulfite aqueous solution was used as the supporting electrolyte in this system. Electrochemical impedance spectroscopy (EIS) was measured by applying 20 mV alternative signal over the frequency ranged from 100 kHz to 10 mHz in the dark. The incident photon to current conversion efficiency (IPCE) was conducted by a PEC-S20 action spectrum measurement system, under the illumination of a 300 W xenon lamp with a monochromator. The IPCE value was calculated given by IPCE(%) = 100(%) × 1240 × I/(λ × J_{light}), where, I is the photocurrent density, λ is the incident light wavelength, and J_{light} is the incident light irradiance. The effective area of the cell was 0.16 cm^{-2} and 0.5 M NaCl aqueous solution was selected as the supporting electrolyte.

3. Results and discussion

3.1. Structure and morphology

Fig. 1 shows XRD patterns of BCN, UCN, CQDs, BCN/CQDs-0.2% and UCN/CQDs-0.2%. The diffraction peaks of both BCN and UCN are well indexed to the g-C_3N_4 (JCPDS Card No. 87-1526). Somewhat differently, the intensity of the (0 0 2) peak of UCN is lower than that of BCN (Fig. 1A), together with a shift in the (0 0 2) peak location from 27.3° for BCN to 27.6° for UCN (Fig. 1B), corresponding to a reduction in the stacking distance of the layer structure from 0.326 nm for BCN to 0.323 nm for UCN. These results implies
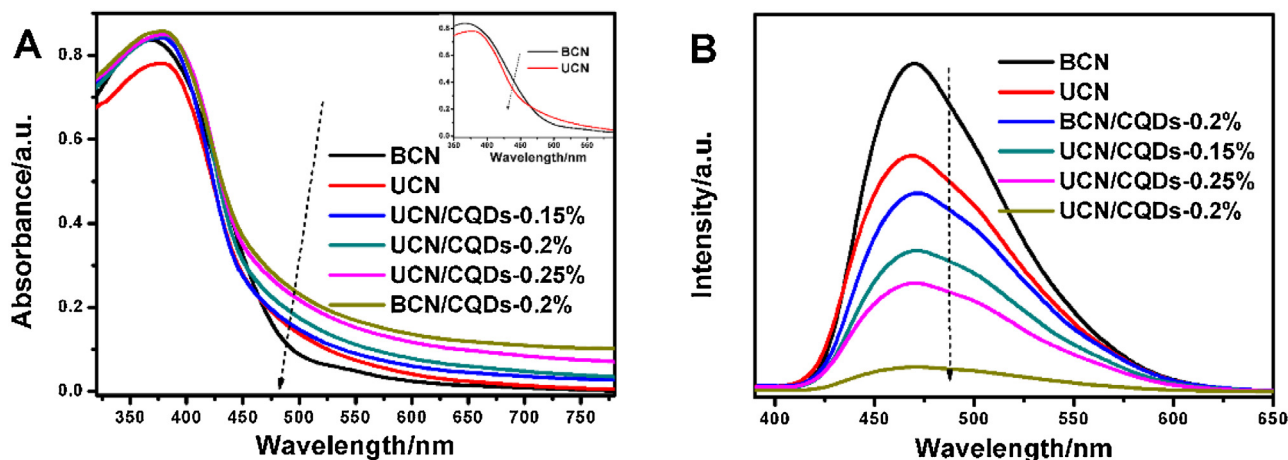
Fig. 5. UV–vis diffuse reflectance spectra (A) and photoluminescence (PL) emission spectra (B) of BCN, UCN, BCN/CQDs-0.2%, UCN/CQDs-0.15%, UCN/CQDs-0.2% and UCN/CQDs-0.25% composites (The excitation wavelength is 375 nm). The inset of (A) is the DRS pattern of BCN and UCN.
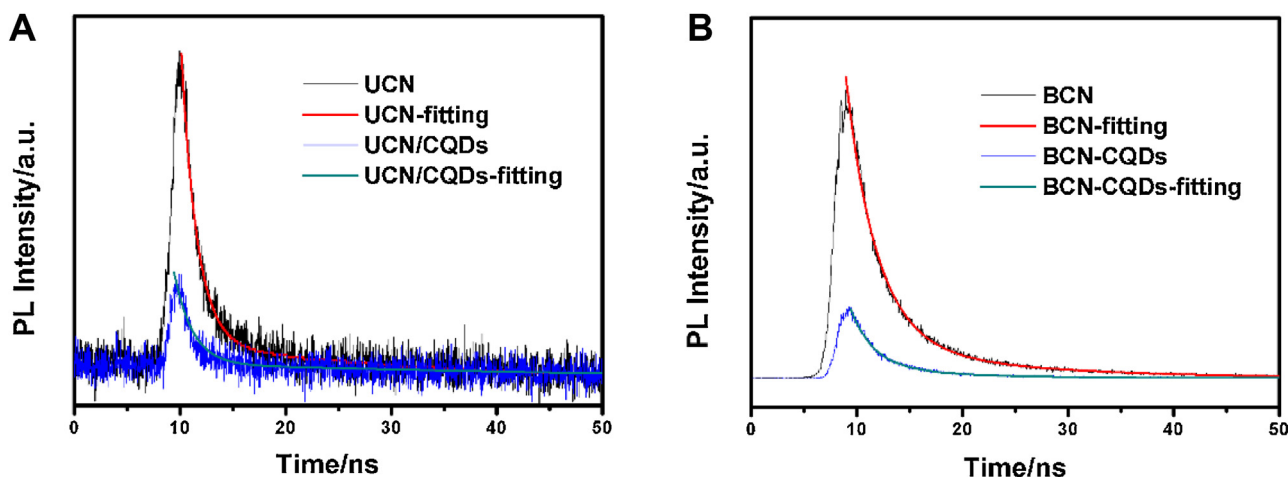

Fig. 6. The time-resolved fluorescence spectra for pristine BCN, BCN/CQDs-0.2%, UCN and UCN/CQDs-0.2% monitored at 470 nm using 375 nm laser at room temperature.

a reduced packing distance between the layered graphene-like plane of g-C3N4, which are ascribed to the denser stacking of UCN after the ammonium chloride thermal blowing process [59,60]. A broad diffraction peak at 20° was found in the XRD pattern of the CQDs, suggesting the CQDs possess poor crystallinity and consist of disordered graphitic-like carbon [61]. The BCN/CQDs-0.2% and UCN/CQDs-0.2% composites show similar patterns as those of BCN and UCN, implying that the structures of UCN and BCN have not been affected by the integration with the CQDs. And no significant diffraction peaks of CQDs can be found in the XRD patterns of BCN/CQDs-0.2% and UCN/CQDs-0.2%, which is contributed to the poor crystallinity of the CQDs or the surperfine CQDs particles very finely dispersed over the surface below the detectable limits of XRD instrument.

Fig. 2 displays the typical FT-IR spectra of CQDs, BCN, UCN, BCN/CQDs-0.2% and UCN/CQDs-0.2%. The FI-IR spectrum of CQDs are similar to that reported previously [58]. While, there are not obvious differences among the FT-IR spectra of BCN, UCN, BCN/CQDs-0.2% and UCN/CQDs-0.2%. Specifically, their spectra show several strong peaks from 1800 to 1400 cm^{-1}, all of which correspond to the distinctive skeletal vibration of the aromatic ring. Whereas the sharp peak at 809 cm^{-1} is considered as the stretching vibration of triazine cycles [62]. Significantly, a small absorption peak at 2180 cm^{-1} is observed in the FT-IR spectra of the BCN/CQDs-0.2% and UCN/CQDs-0.2% samples, while it is almost absent in those

of BCN and UCN. This peak could be considered to be originated from the inclusion defective sites and might be taken as an indicator that CQDs have been successfully coupled with g-C$_3$N$_4$ [63].

Fig. 3 displays TEM images of BCN, UCN, CQDs, BCN/CQDs-0.2% and UCN/CQDs-0.2%. Compared to BCN with a compact microstructure (Fig. 3A), the as-prepared UCN sample consists of the ultrathin two-dimension layers with abundant of pores, originated from the gases release from NH$_4$Cl during the high temperature calcination of the precursors [16]. The difference in morphology and microstructure between BCN and UCN are also observed from their SEM images (Fig. S1, Supporting information), compared with BCN, UCN presents a loose mesh structure and consists of overlap nanosheets with lamellar morphology. Moreover, their N$_2$ sorption–desorption isotherms and Barrett-Joyner-Halenda (BJH) pore size distributions are shown in Fig. S2. The specific surface area and pore volume of UCN has been measured to be 35.315 m^2/g and 0.21 cm^3/g, which is largely higher than 3.918 m^2/g and 0.03 cm^3/g of BCN. The enhanced specific surface area and pore volume of UCN could provide more active sites and shorten the distance of mass transfer, thus facilitating the photocatalytic activity of UCN. As displayed in Fig. 3C and D, the CQDs are uniformly distributed, and no aggregation of the nanoparticles can be observed. The particle sizes of the CQDs range from 2 nm to 5 nm (Fig. S3), and the average diameter has been estimated to be 2.69 nm. And it can be seen from the digital photographs (the inset of Fig. 3C) that the as-obtained CQDs
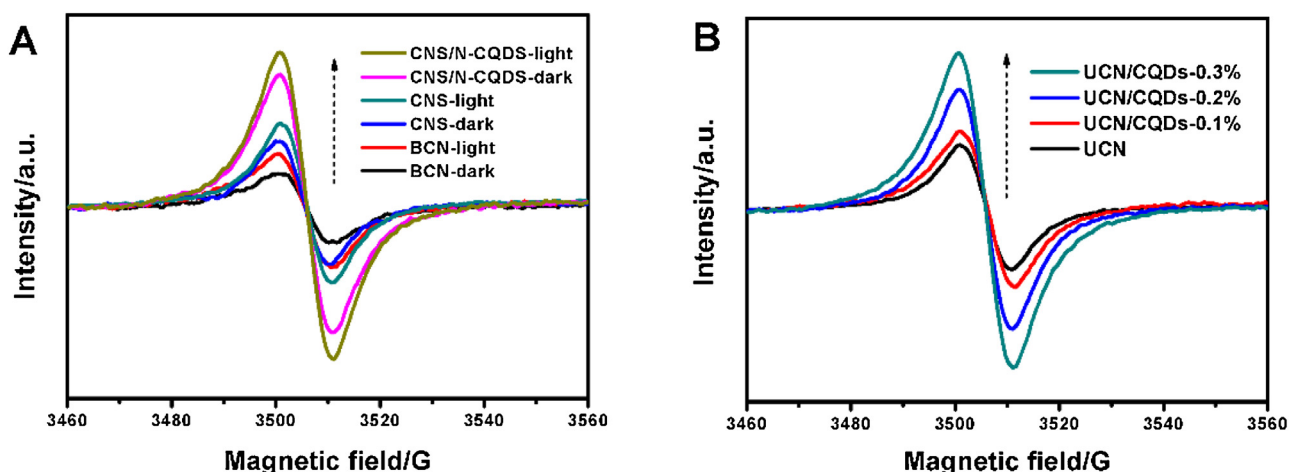
Fig. 7. Room-temperature UV–vis Solid-state EPR spectra of (A) BCN, UCN, BCN/CQDs-0.2% and UCN/CQDs-0.2% with visible light (λ > 420 nm) or in the dark, (B) UCN/CQDs-x% samples in visible light irradiation.
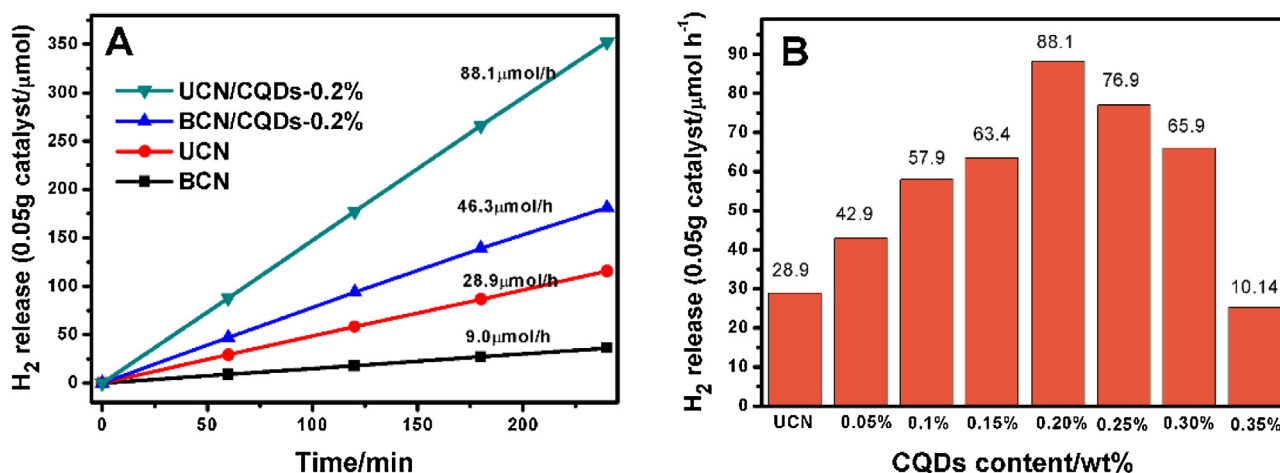

Fig. 8. photocatalytic activity of (A) BCN, UCN, BCN/CQDs-0.2% and UCN/CQDs-0.2%, (B) different CQDs content of UCN/CQDs-x% comparison for the HER under visible light irradiation (>420 nm).

solution exhibits a homogeneous phase without any precipitations, indicating the good dispersion of the CQDs in water. The TEM and HRTEM images of BCN/CQDs-0.2% and UCN/CQDs-0.2% (Fig. 3E–H) clearly indicate the presence of the CQDs on the surfaces of BCN and UCN. More significantly, a difference in particle size of the CQDs are found between BCN/CQDs-0.2% and UCN/CQDs-0.2% that the CQDs attached on BCN (Fig. 3E) are larger than those anchored on UCN (Fig. 3G). While the particle size of the CQDs anchored on UCN are almost the same as that of those in the as-prepared suspension (Fig. 3C). These results reveal that particle aggregation have occurred when the CQDs are coupled with BCN, while the aggregation does not happen during the coupling of the CQDs with UCN. It is implied that the lamellar structure of UCN may facilitate the π-π stacking interactions between CQDs and UCN [64]. In addition, a diffuse ring pattern is observed from the selected area electron diffraction (SEAD) of the CQDs anchored on UCN (the insert of Fig. 3H), indicating the amorphous phase of the CQDs. This result can be used to explain the absence of diffraction peaks for the CQDs in the XRD patterns of BCN/CQDs-0.2% and UCN/CQDs-0.2%.

From the XPS pattern of UCN/CQDs-0.2% shown in Fig. 4, only C, N, O three elements are investigated in the survey spectrum (Fig. 4A). The C 1s spectrum (Fig. 4B) exhibits a broad peak of C—C at 284.5 eV. The peaks at 287.4 eV and 287.8 eV belong to C—N and C=O, respectively. With regards to N 1s spectrum (Fig. 4C),

it presents three characteristic peaks of nitrogen states including pyridinic-N (397.7 eV), triazine rings C—N—C (399.5 eV) and tertiary nitrogen N—(C)$_3$ in heptazine unit (400.6 eV). It is inferred that these three N units compose the basic units of g-C$_3$N$_4$, which are similar to those in reported literature [32]. The peaks of O 1s at 531.1 eV and 532.9 eV correspond to C—O and C=O, respectively. By comparing the XPS results between pristine UCN (Fig. S4) and UCN/CQDs, it reveals that the element chemical state and content of UCN is almost unchanged after the couple of CQDs with UCN.

3.2. Optical properties

Fig. 5 shows the DRS of the prepared materials. Compared with BCN (Fig. 5A), UCN exhibits a slightly blue shift in the absorption edge, which could be attributed to the quantum confinement induced by the ultrathin g-C$_3$N$_4$ nanosheets [65]. Moreover, UCN exhibits enhanced optical absorption in the visible light region between 470 nm and 600 nm than BCN, which might be attributed to the multiple reflections of incoming light within the pores in the nanosheets [63]. For the UCN/CQDs composites with different mass fractions of CQDs, it is found that the coupling with CQDs extends the optical absorption of UCN to the near IR region, and their visible light absorption increases with the mass fraction of CQDs. Moreover, BCN/CQDs-0.2% shows higher optical absorption
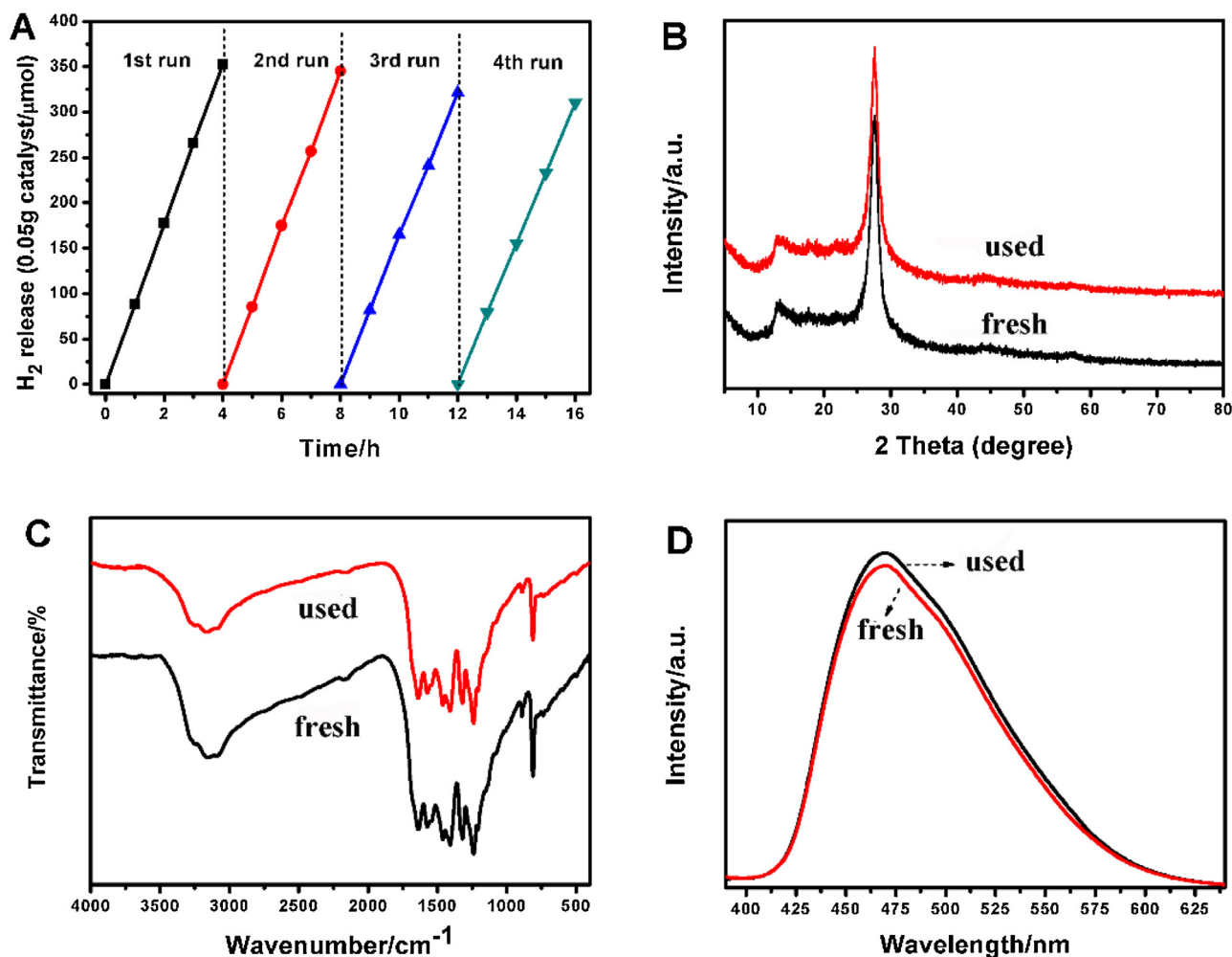
Fig. 9. (A) Time course of H_2 release for UCN/CQDs-0.2% under visible light irradiation ($\lambda > 420$ nm). (Degassing the closed gas circulation system again for 30 min and then turning on the light source after the end of one cycle), (B) XRD pattern, (C) FTIR spectra and (D) PL spectra of fresh and used UCN/CQDs-0.2% composites.
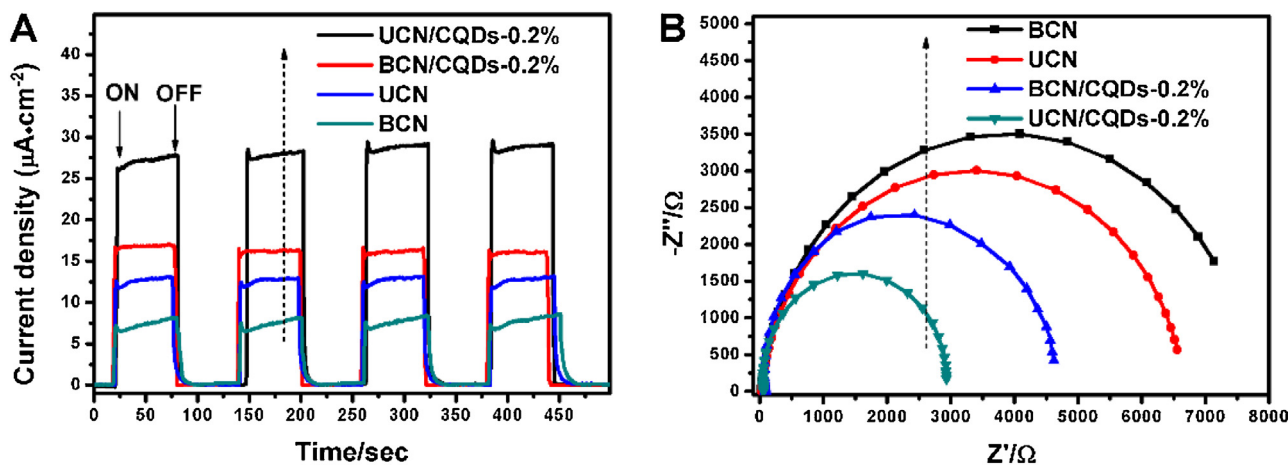

Fig. 10. Photoelectrochemical properties of BCN, UCN, BCN/CQDs-0.2% and UCN/CQDs-0.2%. (A) Periodic ON/OFF photocurrent response in 0.25 M Na_2S/0.35 M Na_2SO_3 electrolyte under visible light irradiation ($\lambda > 420$ nm) at 0.5 V vs. Ag/AgCl electrode and (B) electrochemical impedance spectroscopy Nyquist plots in the dark.

as compared with UCN/CQDs-0.2%, which might originate from the difference in particle size of the carbon dots anchored on BCN and UCN, as revealed by TEM observations (Fig. 3E and G).

The photoluminescence (PL) spectra of the obtained samples have been obtained for investigating their charge separation and recombination behavior, as displayed in Fig. 5B. Compared with

BCN, UCN exhibits reduced PL intensity, suggesting that less charge recombination occurred in UCN. This result implies that the two dimension lamellar structure along with the enhanced specific surface area and pore volume accelerates the charge transport in UCN, resulting in the less charge recombination. For the UCN-CQDs composites with different mass fractions of CQDs, all of them show
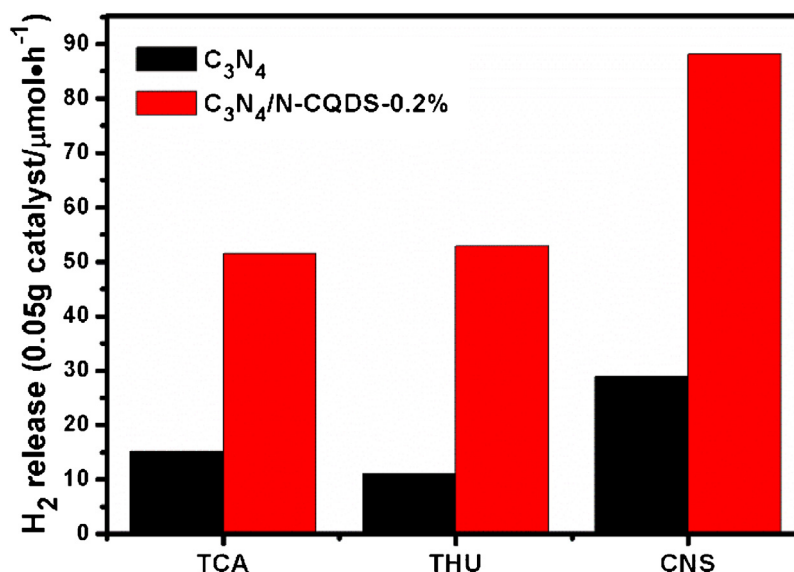
Fig. 11. The photocatalytic performance of C_3N_4 and C_3N_4/CQDs-0.2% form the different precursors for the H2 release rate under visible light irradiation (TCA: trithiocyanuric acid, THU: thiourea, UCN: dicyandiamide and ammonium chloride).

Table 1

The fluorescence decay lifetimes and their percentages of photo-induced carriers in the pristine BCN, BCN/CQDs-0.2%, UCN and UCN/CQDs-0.2% composites.

	τ_1/ns	Rel (%)	τ_2/ns	Rel (%)	τ/ns
BCN	1.50	36.65	19.24	63.35	12.74
BCN/CQDs	1.45	34.53	32.62	65.47	21.85
UCN	1.49	36.58	20.32	63.42	13.43
UCN/CQDs	1.44	32.42	37.45	65.58	25.02

reduced PL intensity as compared with UCN, revealing that the coupling with CQDs plays a role in suppressing the recombination of the photogenerated carriers. And the PL intensity of the UCN-CQDs composites reduce as the mass fraction of CQDs increase from 0.15% to 0.2%, and then enhance with the further increasing in mass fraction from 0.2% to 0.25%. It is revealed that UCN/CQDs-0.2% exhibits the lowest PL intensity, suggesting its least charge recombination. More significantly, the PL intensity of UCN/CQDs-0.2% is much lower than that of BCN/CQDs-0.2%, implying that the π-π stacking interactions between CQDs and UCN greatly suppress the charge recombination by forming a type-II van der Waals heterojunction [55].

The lifetime of photo-induced carriers of the time-resolved fluorescence spectra for pristine UCN and UCN/CQDs-0.2% were further investigated at 470 nm using 375 nm laser at room temperature, as shown in Fig. 6. And the fitting decay spectra of the radiative lifetimes with different percentages are listed in Table 1. The short life time of charge carriers in UCN/CQDs-0.2% is 1.44 ns with the percentage of 32.42% compared to 1.49 ns and 36.58% in UCN. Both the long life time and percentage of photo-induced carriers increase from 20.32 ns and 63.42% in UCN to 37.45 ns and 65.58% in UCN/CQDs-0.2%, respectively. And the weighted mean lifetime of 25.02 ns for UCN/CQDs-0.2% is much larger than 13.42 ns for UCN. In addition, BCN/CQDs-0.2% also exhibits the longer life time than BCN. Hence, these results of the extended lifetime of photo-induced carriers over UCN/CQDs-0.2% and BCN/CQDs-0.2% samples do further illustrate the introduction of CQDs can efficiently retard the carriers recombination and enhance the possibility of charge carriers participating in photocatalytic water splitting. When compared the lifetime of photo-generated carriers between UCN/CQDs-0.2% and BCN/CQDs-0.2%, it can be seen UCN/CQDs-0.2% presents the

superior value, which is contributed to the enhanced specific surface area.

In addition, room temperature electron paramagnetic resonance (EPR) technology has been employed to investigate the electronic band structure of the prepared samples. As shown in Fig. 7A, only one single Lorentzian lines centered at 3505 G with a g value of 2.0027 is observed for all the g-C_3N_4-based samples. It is attributed to the unpaired electrons of carbon atoms with the odds numbers in aromatic rings or π-π conjugation bonding nanosized clusters on the surface of CN texture, demonstrating a well established semiconductors structure [32,66,67]. The EPR intensity of BCN/CQDs-0.2% and UCN/CQDs-0.2% are larger than that of BCN and UCN samples in the dark, suggesting a greater delocalization and mobility of the spins leading to higher charge carriers density [68]. And the signal intension of UCN/CQDs-0.2% exceeds that of BCN/CQDs-0.2%, ascribing to the enhanced specific surface area and pore volume among UCN. Under visible light irradiation, the intensity of EPR of UCN/CQDs-0.2% is further enhanced, verifying the efficient generation of photo-induced carrier pairs. What's more, as displayed in Fig. 7B, the intensity of ERP signal is gradually increased as raising the CQDs content coupled with UCN, which is ascribed to π-π conjugation between UCN and CQDs. Consequently, it is implied that the couple of CQDs with UCN would effectively facilitate the photo-induced carriers generation in essence, which is consistent with the aforementioned results.

3.3. Photocatalytic activity

The photocatalytic activity of as-obtained samples has been evaluated by H_2 release reactions from 5% methanol aqueous under visible light irradiation ($\lambda > 420$ nm), in which 0.2% wt H_2PtCl_6 was used as cocatalyst. As shown in Fig. 8A, UCN shows an enhanced photocatalytic H_2 evolution rate (HER, 28.9 μmol/h) and is 3.2 times of BCN (9.0 μmol/h), owing to the increased specific surface area and the optimized two-dimension structures. And compared to UCN, as expected, the HER of the UCN/CQDs-0.2% (88.1 μmol/h) is 3.05 folds of it and BCN/CQDs-0.2% (46.3 μmol/h) is 5.14 folds of BCN indicating the incorporation of CQDs into g-C3N4 have a profound effect on the photocatalytic performance. Moreover, the HER of different amounts CQDs coupled with UCN are also conducted (Fig. 8B), the HER gradually enhances with the increase of
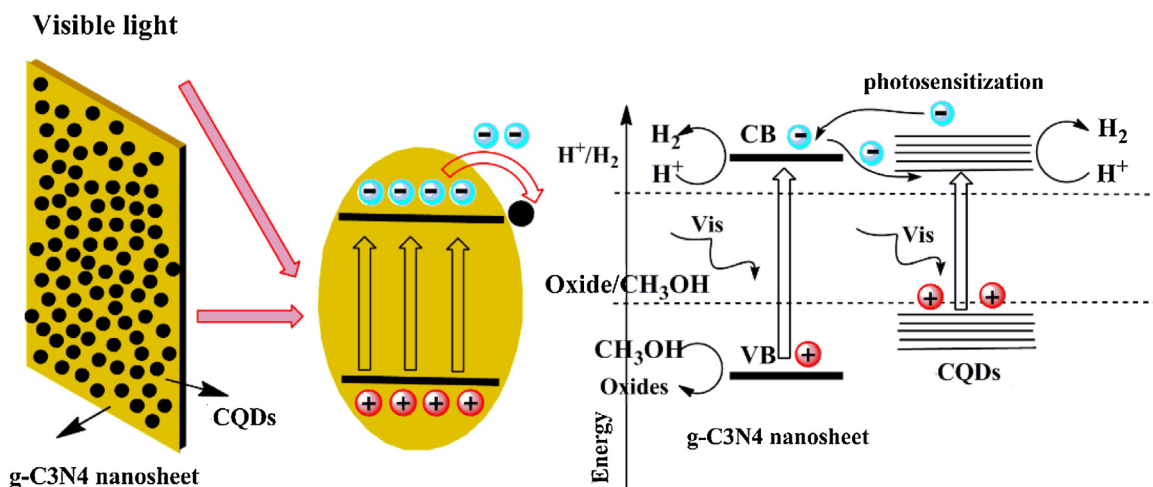
Fig. 12. Schematic illustration for the photocatalytic process of UCN/CQDs photocatalysts under visible light irradiation ($\lambda > 420$ nm).

CQDs concentration. The highest HER (88.1 μmol/h) is observed for UCN/CQDs-0.2%, then the HER decreases as with the excessive CQDs addition. The increase tendency of HER is accorded with the PL results, suggesting the reaction primarily proceeded via the retarded recombination of photo-induced carriers. To further confirm the main driving force of the photocatalytic activity, the comparison in the wavelength dependence of H_2 release rate between UCN/CQDs-0.2% and UCN is obtained in Fig. S5. For the UCN/CQDs-0.2% composite, somewhat differently, it is found that the HER is not coincidence with the optical absorption region, and the HER (17.6 μmol/h) on $\lambda = 465 \pm 20$ nm is much larger than on $\lambda = 420 \pm 20$ nm, suggesting the absorption of the visible photons is not the main role in the photocatalytic performance [54]. And for the comparison between UCN/CQDs-0.2% and UCN, the HER of UCN/CQDs-0.2% is obvious higher than UCN under different wavelength irradiation, further confirming the incorporation of CQDs would effectively facilitate the photocatalytic activity. Notably, the UCN/CQDs-0.2% composite shows visible light response under $\lambda = 510 \pm 20$ nm, while UCN exhibit no hydrogen release. Moreover, in order to further investigate their photocatalytic performance as a function of the irradiation light wavelength, the incident photon to current conversion efficiency (IPCE) was conducted, as shown in Fig. S6. Both UCN/CQDs-0.2% and UCN have an photo-response in the wavelength range between 400 and 500 nm, while it is clear UCN/CQDs-0.2% photoelectrode shows the higher value than UCN. And the maximum IPCE value for UCN/CQDs-0.2% has been obtained at 450 nm, consistent with the HER under different wavelength irradiation.

On one hand, it is attributed that CQDs could be used as a photosensitizer, which just like organic dyes to sensitize UCN and donate the photo-induced electrons to the conduction band of UCN, leading to the extended visible light response region for photocatalytic H_2 release. On the other hand, as shown in Fig. S7, the CQDs process upconversion photoluminescence properties, leading to absorb longer wavelength visible light upon illumination and emit the shorter light. Under different wavelengths excitation from 720 nm to 880 nm, the position of PL peaks are almost unchanged and exhibit a strong peak around 510 nm. The increase in optical absorption could result in more photo-induced carriers formed and promote the visible light driven photocatalytic activity [56].

In addition, the comparison over the photocatalytic activity of UCN/CQDs-0.2% with that of the same weigh physical mixture of the UCN and CQDs-0.2% was also investigated. As observed from Fig. S8, the HER of the physical mixture UCN and CQDs-0.2% is much lower than UCN/CQDs-0.2% or even weaker than pristine UCN, imply-

ing the CQDs efficiently integrated into UCN are necessary for the high photocatalytic activity. Note that the pure CQDs display no photocatalytic activity for hydrogen release under visible light irradiation. The photocatalytic activity of UCN and UCN-hydrothermal (under the identical condition for preparing UCN/CQDs composites but without adding CQDs) was also investigated, as shown in Fig. S9, they exhibit almost the same HER, indicating the hydrothermal process does not alter the photocatalytic performance.

To verify the stability of the photocatalyst, the time course of H_2 release over UCN/CQDs-0.2% has been carried out (Fig. 9). Under 4 h continuous illumination, the amount of H_2 release enhances linearly. And after 4 cycles H_2 release experiments, the HER does not exhibit any obvious deactivation, suggesting the robust stability of the UCN/CQDs-0.2% composite. In addition, the comparisons in both structures and morphologies between the fresh and recycled samples have been further carried out by XRD, FT-IR, PL and SEM characterization methods. The XRD and FT-IR patterns in Fig. 9B and C indicate no distinct change is found for the recycled samples, verifying the structure of catalysts could maintain almost no alteration after the photocatalytic reaction. As shown in Fig. 9D, both samples nearly present the same intensity of the PL peak under identical condition, which is derived from the well retained electronic structure and surface heterostructures of UCN/CQDs after reaction. And from the TEM images of UCN/CQDs after the reaction (Fig. S10), we can find many nano particles well dispersed onto the surface of the UCN, and the sizes of the particles range from 2 nm–5 nm. And as the CQDs and the Pt particles may retain the similar size and the alike shape, it is difficult to distinguish these two components. However, it is clear to observe that the Pt particles exhibit homogeneous distribution onto the photocatalyst after reaction from the STEM images (Fig. S10C), demonstrating the successful reduction from Pt^{4+} to metal Pt under the in-situ photodeposition method.

The electrochemical experiment has been conducted to further investigate the photo-induced charge transfer and separation behaviors. As shown in Fig. 10A, the transient photoelectrochemical response measurement is recorded over the obtained samples under visible light irradiation. As expected, UCN shows a larger value than BCN, and UCN/CQDs-0.2% exhibits the highest photocurrent intensity (almost 1.55, 2.2 and 3.8 folds of BCN/CQDs-0.2%, UCN and BCN, respectively). The increasing photocurrent value of UCN/CQDs-0.2% indicates the more efficient photogenerated charge generation, which means the higher separation and transfer efficiency of the photo-induced carriers [69,70]. Moreover, after repeated four ON/OFF illumination cycles, the transient photocurrent among photocatalyst samples almost maintain reversibly and

reproducibly, implying the good photoelectrochemical stability. In Fig. 10B, it is clear that an obvious decrease for UCN/CQDs-0.2% in semicircular Nyquist plots is observed in the dark when compared to BCN/CQDs-0.2%, BCN and UCN, which is attributed to the improved electronic conductivity [33,41]. This result is consistent with the tendency of photocurrent response, clearly demonstrating the incorporation of CQDs into CN nanosheets texture could effectively facilitate the photo-induced charge transfer and separation, which leads to the obvious enhanced photocatalytic hydrogen release.

Moreover, to further verify the versatility of the method that CQDs coupled with carbon nitride photocatalyst could effectively raise the photocatalyst performance, other two typical precursor, trithiocyanuric acid (TCA) and thiourea (THU), for C_3N_4 synthesis were picked out and used to prepare the C_3N_4/CQDs-0.2% composites under the identical prepared procedures as with the UCN/CQDs-0.2%. The results of HER are presented in Fig. 11. Obviously, the obtained C_3N_4/CQDs-0.2% composites prepared from TCA and THU exhibit the higher value than that of the pristine C_3N_4, and UCN/CQDs-0.2% still shows the better HER value than others. Therefore, it is tentatively concluded that coupling with the CQDs form bee pollens to prepare semiconductor composites can be a feasible way to advance the photocatalytic activity. What's more, it is worth to point out that the ultrathin 2D nanosheets coupled with 0D CQDs would gain better photocatalytic activity performance than the bulk materials.

Based on the above results, a tentative mechanism for enhancing photocatalytic performance among UCN/CQDs composites are proposed, as illustrated in Fig. 12. Firstly, CQDs serve as an electron acceptor, and the photo-induced electrons excited from UCN under visible light can be shuttled freely to the conducting texture of CQDs, consequently, efficiently retarding the recombination and prolonging the lifetime of electron-hole pairs. Secondly, the π-conjugation CQDs are used as a photosensitizer like organic dyes to sensitize UCN and donate the electrons to the conduction band of UCN, resulting in the extended visible light response region for photocatalytic H_2 release. Lastly, as CQDs process upconversion photoluminescence properties, they are capable of absorbing a longer wavelength visible light and then emit the shorter wavelength light, leading to exciting UCN to form more charge carriers. But it is worth pointing out that, as the yield of photocatalytic hydrogen production is well consistent with the PL results, the photogenerated charge-separation efficiency serve as the main factor for the photocatalytic activity of UCN/CQDs composites. Thus, the drawback of fast charge carriers recombination in CN photocatalysts have been efficiently suppressed by the construction of 2D/0D heterostructures, and a better photocatalytic performance is obtained.

4. Conclusions

In summary, we have further developed the strategy of the assembly of 2D/0D UCN/CQDs photocatalyst by the hydrothermal method, and the visible light absorption and the photo-induced carriers separation/mobility of UCN/CQDs have been significantly enhanced. The retarded recombination of charge carriers is believed to play a primary role for their remarkably increased hydrogen release activity. Under the visible light irradiation, the obtained H_2 revolution rate of UCN/CQDs-0.2% is 9.79, 3.05 and 1.91 times of pristine BCN, UCN and BCN/CQDs-0.2%, respectively. Also UCN/CQDs-0.2% composites exhibit good stability for long term irradiation. This work may provide a simple and common process for constructing novel carbon nanodots material coupled with CN frameworks for increasing its photocatalytic performance.

Appendix A. Supplementary data

Supplementary data associated with this article can be found, in the online version, at http://dx.doi.org/10.1016/j.apcatb.2016.04.034.

References

[1] R. Asahi, T. Morikawa, T. Ohwaki, K. Aoki, Y. Taga, Science 293 (2001) 269–271.
[2] A. Kudo, Y. Miseki, Chem. Soc. Rev. 38 (2009) 253–278.
[3] Z.G. Zou, J.H. Ye, K. Sayama, H. Arakawa, Nature 414 (2001) 625–627.
[4] X. Chen, L. Liu, P.Y. Yu, S.S. Mao, Science 331 (2011) 746–750.
[5] K. Maeda, K. Teramura, D.L. Lu, T. Takata, N. Saito, Y. Inoue, K. Domen, Nature 440 (2006) 295.
[6] T. Hisatomi, J. Kubota, K. Domen, Chem. Soc. Rev. 43 (2014) 7520–7535.
[7] K. Maeda, T. Takata, M. Hara, N. Saito, Y. Inoue, H. Kobayashi, K. Domen, J. Am. Chem. Soc. 127 (2005) 8286–8287.
[8] T. Ohno, L. Bai, T. Hisatomi, K. Maeda, K. Domen, J. Am. Chem. Soc. 134 (2012) 8254–8259.
[9] K. Chang, Z. Mei, T. Wang, Q. Kang, S. Ouyang, J. Ye, Acs Nano 8 (2014) 7078–7087.
[10] F.-X. Xiao, J. Miao, B. Liu, J. Am. Chem. Soc. 136 (2014) 1559–1569.
[11] J. Zhang, J. Yu, M. Jaroniec, J.R. Gong, Nano Lett. 12 (2012) 4584–4589.
[12] K. Maeda, M. Higashi, D. Lu, R. Abe, K. Domen, J. Am. Chem. Soc. 132 (2010) 5858–5868.
[13] K. Maeda, K. Domen, J. Phys. Chem. C 111 (2007) 7851–7861.
[14] S. Cao, J. Low, J. Yu, M. Jaroniec, Adv. Mater. 27 (2015) 2150–2176.
[15] S. Yang, Y. Gong, J. Zhang, L. Zhan, L. Ma, Z. Fang, R. Vajtai, X. Wang, P.M. Ajayan, Adv. Mater. 25 (2013) 2452–2456.
[16] X. Lu, K. Xu, P. Chen, K. Jia, S. Liu, C. Wu, J. Mater. Chem. A 2 (2014) 18924–18928.
[17] P. Niu, L. Zhang, G. Liu, H.-M. Cheng, Adv. Funct. Mater. 22 (2012) 4763–4770.
[18] X. Wang, K. Maeda, A. Thomas, K. Takanabe, G. Xin, J.M. Carlsson, K. Domen, M. Antonietti, Nat. Mater. 8 (2009) 76–80.
[19] J. Zhang, Y. Chen, X. Wang, Energy Environ. Sci. 8 (2015) 3092–3108.
[20] X. Wang, S. Blechert, M. Antonietti, ACS Catal. 2 (2012) 1596–1606.
[21] Y. Wang, X. Wang, M. Antonietti, Angew. Chem.-Int. Ed. 51 (2012) 68–89.
[22] X. Chen, J. Zhang, X. Fu, M. Antonietti, X. Wang, J. Am. Chem. Soc. 131 (2009) 11658–11659.
[23] Q. Liu, J. Zhang, Langmuir 29 (2013) 3821–3828.
[24] S. Tonda, S. Kumar, S. Kandula, V. Shanker, J. Mater. Chem. A 2 (2014) 6772–6780.
[25] M. Zhang, X. Bai, D. Liu, J. Wang, Y. Zhu, Appl. Catal. B 164 (2015) 77–81.
[26] Y.-P. Zhu, T.-Z. Ren, Z.-Y. Yuana, ACS Appl. Mater. Interfaces 7 (2015) 16850–16856.
[27] Y. Zhou, L. Zhang, J. Liu, X. Fan, B. Wang, M. Wang, W. Ren, J. Wang, M. Li, J. Shi, J. Mater. Chem. A 3 (2015) 3862–3867.
[28] Y.-P. Zhu, M. Li, Y.-L. Liu, T.-Z. Ren, Z.-Y. Yuan, J. Phys. Chem. C 118 (2014) 10963–10971.
[29] G. Liu, P. Niu, C. Sun, S.C. Smith, Z. Chen, G.Q. Lu, H.-M. Cheng, J. Am. Chem. Soc. 132 (2010) 11642–11648.
[30] W.-J. Ong, L.K. Putri, L.-L. Tan, S.-P. Chai, S.-T. Yong, Appl. Catal. B 180 (2016) 530–543.
[31] W. Zhao, Z. Wei, H. He, J. Xu, J. Li, S. Yang, C. Sun, Appl. Catal. A 501 (2015) 74–82.
[32] J. Qin, S. Wang, H. Ren, Y. Hou, X. Wang, Appl. Catal. B: Environ. 179 (2015) 1–8.
[33] Z. Chen, P. Sun, B. Fan, Q. Liu, Z. Zhang, X. Fang, Appl. Catal. B: Environ. 170 (2015) 10–16.
[34] X. Zhang, T. Peng, L. Yu, R. Li, Q. Li, Z. Li, ACS Catal. 5 (2015) 504–510.
[35] G. Zhang, C. Huang, X. Wang, Small 11 (2015) 1215–1221.
[36] Y. Ma, X. Wang, Y. Jia, X. Chen, H. Han, C. Li, Chem. Rev. 114 (2014) 9987–10043.
[37] P. Zhou, J. Yu, M. Jaroniec, Adv. Mater. 26 (2014) 4920–4935.
[38] Z. Lin, X. Wang, Angew. Chem. Int. Ed. Engl. 52 (2013) 1735–1738.
[39] J. Zhang, G. Zhang, X. Chen, S. Lin, L. Möhlmann, G. Dołęga, G. Lipner, M. Antonietti, S. Blechert, X. Wang, Angew. Chem. 124 (2012) 3237–3241.
[40] M. Zhang, X. Wang, Energy Environ. Sci. 7 (2014) 1902–1906.
[41] X. Fan, L. Zhang, M. Wang, W. Huang, Y. Zhou, M. Li, R. Cheng, J. Shi, Appl. Catal. B: Environ. 182 (2016) 68–73.
[42] Y. Ma, X. Wang, Y. Jia, X. Chen, H. Han, C. Li, Chem. Rev. 114 (2014) 9987–10043.
[43] H. Li, X. He, Z. Kang, H. Huang, Y. Liu, J. Liu, S. Lian, C.H.A. Tsang, X. Yang, S.T. Lee, Angew. Chem. Int. Ed. 49 (2010) 4430–4434.
[44] X. Li, M. Rui, J. Song, Z. Shen, H. Zeng, Adv. Funct. Mater. 25 (2015) 4929–4947.
[45] S. Zhuo, M. Shao, S.-T. Lee, ACS Nano 6 (2012) 1059–1064.
[46] H. Li, Z. Kang, Y. Liu, S.-T. Lee, J. Mater. Chem. 22 (2012) 24230.

[47] X. Zhang, F. Wang, H. Huang, H. Li, X. Han, Y. Liu, Z. Kang, Nanoscale 5 (2013) 2274.

[48] H. Yu, Y. Zhao, C. Zhou, L. Shang, Y. Peng, Y. Cao, L.-Z. Wu, C.-H. Tung, T. Zhang, J. Mater. Chem. A 2 (2014) 3344.

[49] N.-N. Chai, H.-X. Wang, C.-X. Hu, Q. Wang, H.-L. Zhang, J. Mater. Chem. A 3 (2015) 16613–16620.

[50] B.Y. Yu, S.-Y. Kwak, J. Mater. Chem. 22 (2012) 8345–8353.

[51] F. Nan, Z. Kang, J. Wang, M. Shen, L. Fang, Appl. Phys. Lett. 106 (2015) 153901.

[52] H. Li, X. Zhang, D.R. MacFarlane, Adv. Energy Mater. 5 (2015).

[53] X. Xia, N. Deng, G. Cui, J. Xie, X. Shi, Y. Zhao, Q. Wang, W. Wang, B. Tang, Chem. Commun. (2015).

[54] J. Liu, Y. Liu, N. Liu, Y. Han, X. Zhang, H. Huang, Y. Lifshitz, S.-T. Lee, J. Zhong, Z. Kang, Science 347 (2015) 970–974.

[55] G. Gao, Y. Jiao, F. Ma, Y. Jiao, E. Waclawik, A. Du, Phys. Chem. Chem. Phys. 17 (2015) 31140–31144.

[56] H. Zhang, L. Zhao, F. Geng, L.-H. Guo, B. Wan, Y. Yang, Appl. Catal. B: Environ. 180 (2016) 656–662.

[57] C. Xu, Q. Han, Y. Zhao, L. Wang, Y. Li, L. Qu, J. Mater. Chem. A 3 (2015) 1841–1846.

[58] J. Zhang, Y. Yuan, G. Liang, S.-H. Yu, Adv. Sci. 2 (2015).

[59] Y. Cui, G. Zhang, Z. Lin, X. Wang, Appl. Catal. B: Environ. 181 (2016) 413–419.

[60] F. Fina, S.K. Callear, G.M. Carins, J.T.S. Irvine, Chem. Mater. 27 (2015) 2612–2618.

[61] Y. Te-Fu, T. Chiao-Yi, C. Shean-Jen, T. Hsisheng, Adv. Mater. 26 (2014) 3297–3303.

[62] Q. Liu, Y. Guo, Z. Chen, Z. Zhang, X. Fang, Appl. Catal. B: Environ. 183 (2016) 231–241.

[63] J. Zhang, M. Zhang, C. Yang, X. Wang, Adv. Mater. 26 (2014) 4121–4126.

[64] X. Wang, L. Wang, F. Zhao, C. Hu, Y. Zhao, Z. Zhang, S. Chen, G. Shi, L. Qu, Nanoscale 7 (2015) 3035–3042.

[65] K. Maeda, R. Kuriki, M. Zhang, X. Wang, O. Ishitani, J. Mater. Chem. A 2 (2014) 15146–15151.

[66] M. Tabbal, T. Christidis, S. Isber, P. Merel, M. El Khakani, M. Chaker, A. Amassian, L. Martinu, J. Appl. Phys. 98 (2005) 4310.

[67] G. Fanchini, S. Ray, A. Tagliaferro, E. Laurenti, Diamond Relat. Mater. 11 (2002) 1143–1148.

[68] S. Stoll, A. Schweiger, J. Magn. Reson. 178 (2006) 42–55.

[69] X. Fan, L. Zhang, R. Cheng, M. Wang, M. Li, Y. Zhou, J. Shi, ACS Catal. 5 (2015) 5008–5015.

[70] G. Zhang, X. Wang, J. Catal. 307 (2013) 246–253.